Flat photonic lattices for near-field imaging with enhanced depth of field

Carlos J. Zapata-Rodríguez,[a] David Pastor,[a] and Juan J. Miret[b]

[b]Departamento de Óptica, Universidad de Valencia, Dr. Moliner 50, 46100 Burjassot, Spain;
[a]Departamento de Óptica, Farmacología y Anatomía, Universidad de Alicante, P.O. Box 99, Alicante, Spain

ABSTRACT

We numerically evaluated the 3D PSF of stratified negative-index superlenses. We determined in terms similar to the Rayleigh criterion the limit of resolution characterizing these image formers. Under some circumstances, the limit of resolution may drop approximately one order of magnitude. We investigated this significant increase of the resolution power in detriment of reducing the depth of field.

Keywords: metamaterials, imaging, superresolution

1. INTRODUCTION

The design of image formers giving rise to stigmatism at least for a conjugate pair is being of extreme interest for long from a practical point of view. The Cartesian ovoid of revolution produces perfect imaging by refraction,[1] whereas a conic section does it in reflection. The case of the plane mirror has been unique until recently since all images without exception are free from monochromatic aberrations. Moreover, a metal-coated flat surface generates a virtual stigmatic image from a three-dimensional (3D) object. With the arrival of negative-refraction-index (NRI) media now we may obtain a real 3D perfect replica back in refraction. Let us remind that Vesselago showed for the first time that a NRI plane-parallel plate will focus radiation from a point source.[2] Also importantly, Pendry pointed out that evanescent waves contribute in addition to the focal volume. This leads to the concept of flat superlenses which demonstrate subwavelength resolution.[3]

Stigmatic imaging might be repeated over and over in stratified NRI devices,[4] which conserve the properties of linearity and 3D shift invariance. On the basis of these two features we formulated the image formation of thick objects by means of a convolution involving the 3D Point Spread Function (PSF) of a single-layer superlens.[5] The scalar 3D PSF is evaluated for p-polarized and s-polarized waves independently and it may be extended to any multilayered medium. This results of convenience for us since the 3D PSF demonstrates high performance to estimate the limit of resolution, for instance, by means of the Rayleigh criterion.

In this paper we apply the 3D PSF to characterize the limit of resolution in the Gaussian image plane and also in out-of-focus planes. The resolution power of flat NRI multilayered superlenses is determined in terms of the number of films and its distribution along the optic axis. Dissipation effects are also discussed. Moreover, when dealing with multiple localized emitters, they are not found necessarily in the same transverse plane though they should be placed in planes very close among themselves in order to produce real images. In relation to this issue we consider the limitations on the depth of field of stratiform image formers.

2. POINT SPREAD FUNCTION

The field distribution generated by a point object may be used to estimate the limit of resolution of a flat superlens. Hakkarainen et al. calculated the PSF of the imaging system by investigating near-field imaging of a point dipole by a lossy, nanoscale metamaterial slab.[6] An alternative method is employed here in order to determine the impulse response. This approach consists of evaluating the PSF produced by a point source which is characterized by a delta function in the object plane (see Ref. 5 for more details).

Further author information: (Send correspondence to C.J.Z.R.)
C.J.Z.R.: E-mail: carlos.zapata@uv.es, Telephone: +34 96 354 38 05

Metamaterials VI, edited by Vladimir Kuzmiak, Peter Markos, Tomasz Szoplik, Proc. of SPIE Vol. 8070
807012 · © 2011 SPIE · CCC code: 0277-786X/11/$18 · doi: 10.1117/12.886458

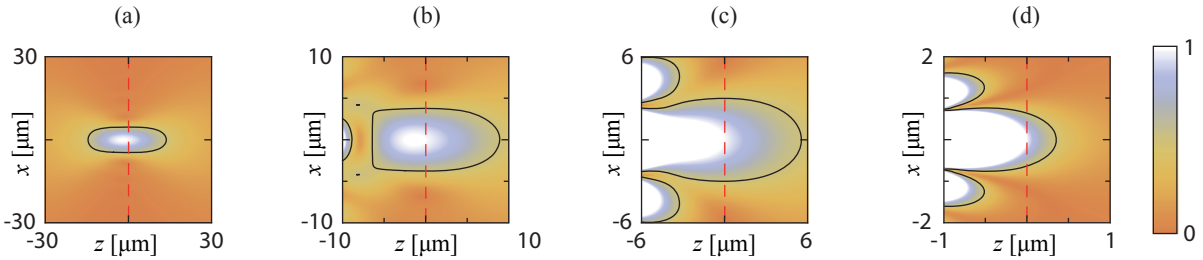

Figure 1. $|h|$ at $\lambda_0 = 10$ μm within $z \geq -d$ for a absorbing films with $\delta = 0.1$ and different widths: (a) $d = 30$ μm, (b) $d = 10$ μm, (c) $d = 6$ μm, and (d) $d = 1$ μm. The density plots are normalized to unity at the geometrical focus $(x, z) = (0, 0)$. The solid line indicates points where amplitude falls off 1/2. The red vertical line marks the focal plane.

Let us consider a NRI medium of width d, relative permittivity and relative permeability $\epsilon_2 = \mu_2 = -1 + i\delta$ for simplicity, where $\delta > 0$ stands for the absorption coefficient. In the surrounding medium $\epsilon_1 = \mu_1 = 1$. Now it is convenient to treat individually p-polarized waves and s-polarized waves. Based on the angular spectrum representation of the scattered field, for s-polarized waves, the field in the image space may be expressed as a 3D convolution in the form of

$$\vec{E}\left(\vec{R}, z\right) = \vec{E}_{sc}\left(\vec{R}, z - 2d\right) * h\left(\vec{R}, z\right), \tag{1}$$

where $\vec{E}_{sc}$ is the electric field excited by the source, and $\vec{R} \perp \hat{z}$. The scalar 3D PSF

$$h\left(\vec{R}, z\right) = \frac{1}{(2\pi)^2} \iint T\left(\vec{k}_\perp\right) \exp\left(i\vec{k}_\perp \vec{R}\right) \exp\left(i\beta_1 z\right) d\vec{k}_\perp, \tag{2}$$

is derived by means of the transmission coefficient between the object plane and the conjugate image plane placed at a distance $2d$,

$$T = \frac{t_{1,2} t_{2,1} e^{i(\beta_1 + \beta_2)d}}{1 - (r_{2,1})^2 e^{2i\beta_2 d}}. \tag{3}$$

The Airy's formula given above depends on the reflection coefficient at a single interface,[7] which yields

$$r_{i,j} = \frac{\mu_j \beta_i - \mu_i \beta_j}{\mu_j \beta_i + \mu_i \beta_j} \tag{4}$$

for TE waves, and the transmission coefficient $t_{i,j} = 1 + r_{i,j}$. Finally the propagation constant

$$\beta_i = \sigma_i \sqrt{\varepsilon_i \mu_i k_0^2 - \vec{k}_\perp^2}, \tag{5}$$

where $\sigma_i = 1$ for dielectrics and $\sigma_i = -1$ for NRI media, k_0 is the wavenumber in vacuum and $\vec{k}_\perp$ is the projection of the wave vector over each flat-lens interface. We point out that $h(\vec{R}, z > 0)$ for $T = 1$, that is for $\delta = 0$, represents the propagator of the first Rayleigh-Sommerfeld integral and it is related with a divergent wave which focus is found in the image plane $z = 0$.[8]

A scalar PSF may be established formally for TM waves by substituting $\vec{E} \to \vec{H}$ and $\mu_i \leftrightarrow \epsilon_i$ concerning the electromagnetic fields and the constitutive parameters of the media. In general the PSFs for s-polarization and p-polarization are different. If $\epsilon_i = \mu_i$, however, the transmission coefficient (3) for both polarizations are alike and therefore their corresponding PSFs are also identical.

The integrand in Eq. (2) is radially symmetric so that the evaluation of the 3D PSF is simplified as

$$h\left(R, z\right) = \frac{1}{2\pi} \int_0^\infty T\left(k_\perp\right) J_0\left(k_\perp R\right) \exp\left(i\beta_1 z\right) k_\perp dk_\perp, \tag{6}$$

where the radial coordinate $R = |\vec{R}|$, and J_0 is the Bessel function of the first kind and of order 0. In Fig. 1 we represent the PSF for a moderate absorption coefficient $\delta = 0.1$ and different widths out of the interval

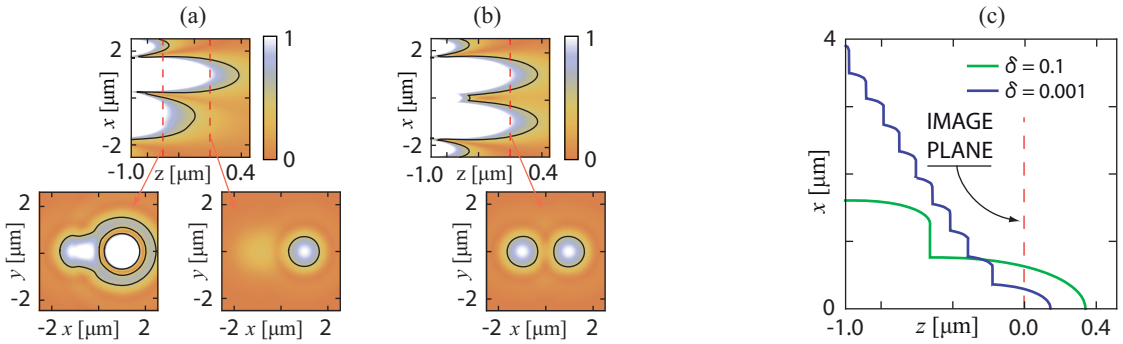

Figure 2. Modulus of the wave field excited by two incoherent point sources after passing through a superlens of $d = 1$ μm and $\delta = 0.1$. In the figure (a) the point object O_1 is 600 nm nearer the lens than O_2. In (b) the two sources are placed in the same transverse plane. (c) Contour of value 1/2 for 3D PSFs corresponding to flat superlenses of different δ.

$z \leq -d$ constituting the virtual image space. The amplitude distribution of the PSF for a slab width d below the wavelength shows a behavior different than the impulse response for $d \gg \lambda_0$. For instance, if $d = 1$ μm, the FWHM of the PSF in the geometrical image plane yields $\Delta_\perp = 1.26$ μm, which is well below the wavelength $\lambda_0 = 10$ μm. Moreover, the amplitude reaches a maximum value in the central point $R = 0$ over the output surface of the lens. Note that in the imaging process, the record of the subwavelength details are associated with spatial frequencies higher than k_0 which fall off fast in the transit from the output plane of the lens toward the image plane, thus frustrating a 3D focusing.[9] On the contrary, when $d = 30$ μm then $\Delta_\perp = 9.00$ μm, which is a value close to λ_0. In this case, the amplitude maximum is found far from the output interface quite close to the image plane. Nevertheless a small axial shift of 1.748 μm is encountered in direction to the lens. Finally the FWHM along the z-axis may be evaluated in this case giving $\Delta_z = 28.3$ μm.

3. LIMIT OF RESOLUTION

In order to determine the limit of resolution making use of the PSF we may find diverse criteria. Perhaps the most known criterion was introduced by Lord Rayleigh,[10] which establishes that two point objects are resolved if the maximum in the diffraction pattern excited by one source lies at least on the first dark ring of the diffraction pattern generated by the second source. Note that for a diffraction pattern in the form of an Airy disk, the limit of resolution coincides with 1.18 times the FWHM of the central peak in intensity. In this paper we consider a similar criterion. Specifically we consider simply the FWHM of the PSF as the limit of resolution of the image-forming system.

For the sake of illustration Figure 2 shows the field intensity produced by two equienergetic point sources in the image space of the flat superlens analyzed in Fig. 1(d). One of the point objects O_1 is placed at $\mathbf{R}'_1 = (1\ \mu\text{m})\ \hat{x}$ and the second point object O_2 is shifted to $\mathbf{R}'_2 = (-1\ \mu\text{m})\ \hat{x}$. To evaluate the intensity distribution we assume that the electromagnetic field is formed by the incoherent superposition of the waves emitted by both sources, putting a stop to spurious interference effects, which is fully consistent with approximations commonly employed in fluorescence microscopy.[11] As a consequence the distribution of intensity is proportional to $\sum_{j=1,2} \left|h(\mathbf{R} - \mathbf{R}'_j, z - z'_j)\right|^2$, where z'_j denotes the location of the two geometrical image planes. Subplots in Fig. 2 are normalized to unity at the image point O'_1, and the solid contours represent an intensity that has fallen down to a value 1/2.

If the point object O_1 remains 600 nm nearer the superlens than O_2, its geometrical image O'_1 is located in a plane ($z'_1 = 0$) further from the output plane of the lens, as shown in Figure 2(a). The presence of the secondary image O'_2 is practically unperceivable in this transverse plane because of the evanescent nature of the image field generated at $z'_2 = -600$ nm. Shifting to the plane of the geometrical image O'_2, it can be caught. However the intensity distribution is superimposed with an intense back tail of the PSF produced by O'_1. Moreover, the contour of intensity 1/2 wrapping around the image point O'_2 in the image plane z'_2 also envelopes the diffraction

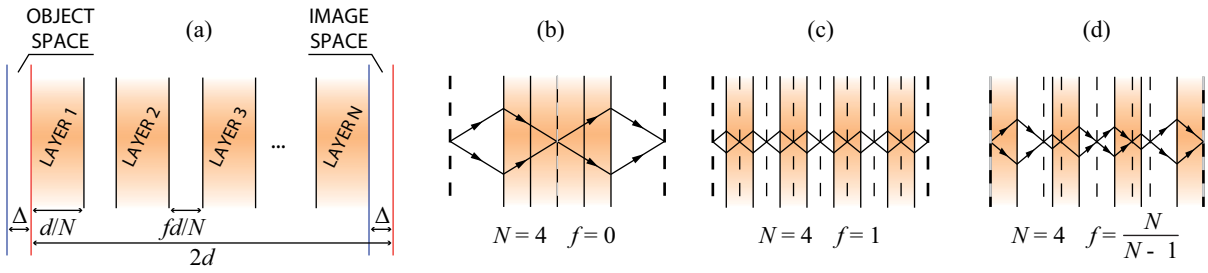

Figure 3. (a) Scheme of a multilayered superlens containing N uniformly-distributed films. We encounter real conjugated pairs simultaneously in the pointed zones, whose width is denoted by Δ. On the right we represent different four-layered superlenses. From (b) to (d), the distance between NRI films increases gradually. Object and final image planes are represented in thick dashed lines, and secondary images are displayed in thin dashed lines.

pattern of O_1'. As a consequence both images are not perfectly resolved. Note that when both sources are coplanar then both images may be resolved, as observed in Fig. 2(b).

The contour of intensity 1/2 corresponding to the normalized 3D PSF for different NRI flat lenses of width $d = 1$ μm is represented in Fig. 2(c). The wavelength $\lambda_0 = 10$ μm remains the same in the numerical simulations. In the geometrical image plane, the film of $\delta = 0.001$ shows a PSF in irradiance with a radius 279 nm, significantly lower than 627 nm attributed to a NRI superlens of $\delta = 0.1$. Such a superresolving behavior is kept in neighboring transverse planes. However, the contribution of intense sidelobes leads to a critical increment of the limit of resolution for $\delta = 0.001$. Moreover, the first lateral peak determines the limit of resolution within the interval -317 nm$< z < -182$ nm, and the second sidelobe is determinant in planes at -417 nm$< z < -317$ nm, up to 8 sidelobes influencing the limit of resolution in the real image space. If $\delta = 0.1$, however, only the first sidelobe may contribute effectively.

4. SUPERRESOLVING MULTILAYERED STRUCTURES

Flat superlenses were conceived originally as an image-forming system composed of a single NRI slab.[2] Note that a silver monolayer also demonstrates the ability of generating an image with subwavelength features.[3] Shortly afterwards it was shown that the limit of resolution of a metallic superlens might be reduced substantially if it is substituted by a set of layers with free-space in between.[12] The amplification of the evanescent wave in the multilayered superlens is significantly lower, so that dissipative effects also diminish. The existence of secondary images in the intermediate spaces allows that new evanescent waves with higher spatial frequency contributes effectively in the formation of the final image, thus improving the resolution power.[4] This idea is being upgrading in recent years[13–16]

A heterogeneous negative-positive index multilayer lens is sketched in Fig. 3. Inside the lensing arrangement N NRI layers are distributed uniformly. Every thin film has a width d/N. Therefore d denotes the resultant length after summing up the widths of the all layers. As a consequence, the distance between the plane of the object and the final geometrical image plane yields $2d$. Note that every interface dielectric-NRI generates an stigmatic image that acts as an object for the next interface, giving $2N - 1$ secondary images. The distance between two adjacent layers is fd/N, being f the proportionality coefficient between the width of each layer and that of free-space in between. The width of the multilayer arrangement e results by summing up N NRI films and $N - 1$ interspaces,

$$e = d\left(1 + f\frac{N-1}{N}\right). \tag{7}$$

In order to generate a real image, the superlens width e should be lower or at least the same than the distance between the object plane and the image plane, $e \leq 2d$. In this case f ranges within the interval $0 \leq f \leq N/(N-1) \leq 2$, being the entire number $N \geq 2$.

Let us point out three cases of special interest. Firstly, if $f = 0$ the set of N films are stacked so that the optical system behaves like a monolayer superlens of width d as shown in Fig. 3(b). When $f = 1$ the NRI films

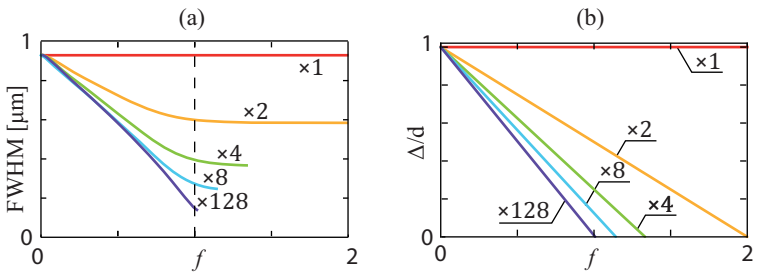

Figure 4. (a) Limit of resolution for flat superlenses of different number N of layers and separation f, keeping $d = 1$ μm fixed. (b) Depth of field normalized to d as a function of f.

and the free space in between coincide in breadth, as illustrated in Fig. 3(c). Finally in the limit $f = N/(N-1)$, the input and output faces of the arrangement are in contact with the object and image planes, respectively. This is depicted in Fig. 3(d).

We estimate the FWHM of the 3D PSF with the conscious aim of evaluating the limit of resolution that corresponds to different multilayered superlenses. Previously, the transmission coefficient T used in Eq. (2) is computed by using the characteristic matrix formulation for isotropic stratified media.[7] In the numerical simulations we use a NRI material with an absorption coefficient $\delta = 0.1$ and total width $d = 1$ μm; also the radiation wavelength is $\lambda_0 = 10$ μm. The results are shown in Fig. 4(a). Within the interval $0 \leq f \leq 1$ the FWHM exhibits a linear decreasing behavior. However its value is maintained constant for $f > 1$. On the other hand, the FWHM decreases if the number N of layers increases up to a saturation limit. In practical terms we may consider that 128 layers represents this limiting case, for which the FWHM is only 141 nm.

The superlens stack becomes an alternative of the monolayer case since the former reduces the limit of resolution significantly. On the contrary this sort of multilayered devices withstand a major difficulty in order to generate real images. The scattering objects should be located closer to the entrance face of the superlens, and as a consequence the conjugate images are found also nearer the output interface. Let us define the depth of field Δ as the width of the two zones where we may encounter real conjugate pairs of objects and images, simultaneously. The depth of field is obtained by considering the distance object-image and subtracting the superlens width, $\Delta = 2d - e$. By utilizing (7) we finally obtain

$$\Delta = d\left(1 - f\frac{N-1}{N}\right). \tag{8}$$

Eq. (8) provides a linear relationship between the depth of field and the distance from adjacent layers. Note that Δ is reduced if the interspace width increases.

The depth of field (8) is depicted in Fig. 4(b) as a function of f for different number N of layers. It is shown that increasing the interspace between layers reduces the depth of field linearly. The slope of these straight lines, $(1-N)/N$, experiences a fast decrement when the number N of layers increases, reaching a limiting value -1. By considering Figs. 4(a) and (b) we conclude that an increase in the number N of layers leads to a reduction of the limit of resolution in detriment of reducing the depth of field, the latter being highly harmful in the formation of 3D images. This tendency is repeated if the interspace between layers increases. Given a specific application, the geometrical coefficient f would be chosen according to the limit of resolution and the depth of field that are necessary for such a practical implementation.

Finally we have computed the 3D PSF and its corresponding transmission coefficient for $N = 4$ nanolayers and different values of f, which are depicted in Fig. 5. The wavelength is set $\lambda_0 = 10$ μm and the parameters characterizing the NRI medium are $d = 1$ μm and $\delta = 0.1$. We observe in the figure that a higher f goes with a transmission coefficient taking significant values within a wider spectral band. This circumstance endorses a narrowing of the central peak pertaining to the 3D PSF, involving a resolution improvement in transverse planes adjacent to focus, $z = 0$. In these lesser-defocused planes sidelobes may be neglected. However evanescent tails grow up with f thus strengthening its presence in planes gradually nearer the focal plane. These sidelong peaks

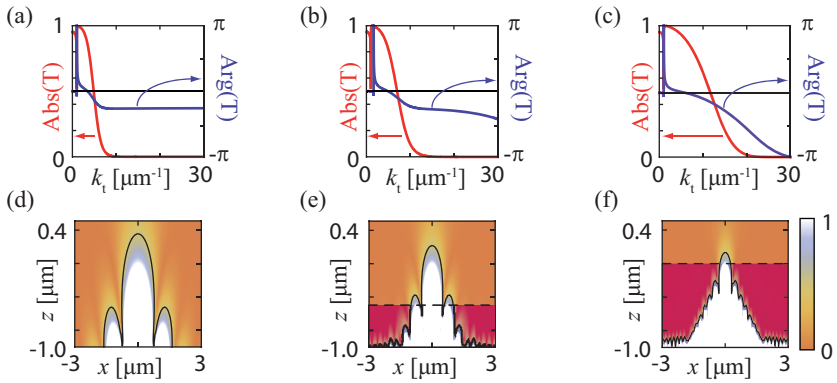

Figure 5. Subfigures (a), (b), and (c) plot the absolute value (red line) and phase (blue line) of the transmission coefficient T for a superlens of $N = 4$ layers and: $f = 0$, $f = 1/2$, and $f = 1$, respectively. Subfigures (d), (e), and (f) show the intensity of the PSF in the meridional plane xz of the image volume related with the superlenses characterized in (a)-(c).

lead to discontinuities in the limit of resolution, which are derived from our criterion of resolution likewise the case $N = 1$ previously analyzed. In particular, the first discontinuity is found at $z = -527$ nm in Fig. 5(d) and it is shifted to $z = -209$ nm in Fig. 5(f). We remind that a higher interspace between layers, that is an increment of f, forces a deterioration of the depth of field. In this sense we have include a dashed line in each subfigure to mark the boundary $z = -\Delta$ delimiting the real image space and the virtual image space. Visually we corroborate that an increment of f leads to a depth-of-field falloff.

5. CONCLUSIONS

We conclude that heterogeneous stratiform superlenses demonstrate an improved resolution power in comparison with image-forming monolayer devices. However this goes with a lower depth of field thus affecting negatively to the observation of images far from the lens exit plane. Therefore, the design of a multilayer superlens involves a trade off between the resolution power required for a given practical implementation and the limitations it includes in the process of recording an image in volume. Finally we point out that the 3D PSF analysis presents potential applications in the complete and simple description of the image formation in stratified metamaterials and 1D photonic crystals. This model is also appropriate for flat-lens designs using metal-dielectric multilayered structures.

ACKNOWLEDGMENTS

This research was funded by the Spanish Ministry of Science and Innovation (MICIIN) under the project TEC2009-11635.

REFERENCES

1. F. L. Pedrotti and L. S. Pedrotti, *Introduction to Optics*, Prentice-Hall, 1993.
2. V. G. Veselago, "The electrodinamics of substances with simultaneously negative values of ϵ and μ," *Physics-Uspekhi* **10**(4), p. 509, 1968.
3. J. B. Pendry, "Negative refraction makes a perfect lens," *Phys. Rev. Lett.* **85**, pp. 3966–3969, 2000.
4. S. A. Ramakrishna, J. B. Pendry, M. C. K. Wiltshire, and W. J. Stewart, "Imaging the near field," *J. Mod. Opt.* **50**, pp. 1419–1430, 2003.
5. C. J. Zapata-Rodríguez, D. Pastor, and J. J. Miret, "Three-dimensional point spread function and generalized amplitude transfer function of near-field flat lenses," *Appl. Opt.* **49**, pp. 5870–5877, 2010.
6. T. Hakkarainen, T. Setälä, and A. T. Friberg, "Subwavelength electromagnetic near-field imaging of point dipole with metamaterial nanoslab," *J. Opt. Soc. Am. A* **26**, pp. 2226–2234, 2009.
7. P. Yeh, *Optical Waves in Layered Media*, Wiley, New York, 1988.

8. M. Nieto-Vesperinas, "Problem of image superresolution with a negative-refractive-index slab," *J. Opt. Soc. Am. A* **21**, pp. 491–498, 2004.
9. R. Marques, M. J. Freire, and J. D. Baena, "Theory of three-dimensional subdiffraction imaging," *Appl. Phys. Lett.* **89**, p. 211113, 2006.
10. M. Born and E. Wolf, *Principles of Optics Seventh (expanded) edition*, Cambridge University Press, 1999.
11. C. Girard and A. Dereux, "Near-field optics theories," *Rep. Prog. Phys.* **59**, pp. 657–699, 1996.
12. E. Shamonina, V. A. Kalinin, K. H. Ringhofer, and L. Solymar, "Imaging, compression and Poynting vector streamlines with negative permittivity materials," *Electron. Lett.* **37**, pp. 1243–1244, 2001.
13. Z. Jaksic and M. Maksimovic, "Ordered artificial nanocomposites for imaging beyond diffraction limit," in *Proc. 1st International Workshop on Nanoscience & Nanotechnology IWON 2005*, pp. 147–156, (Belgrade), Nov. 2005.
14. B. Wood, J. B. Pendry, and D. P. Tsai, "Directed subwavelength imaging using a layered metal-dielectric system," *Phys. Rev. B* **74**, p. 115116, 2006.
15. D. de Ceglia, M. A. Vincenti, M. G. Cappeddu, M. Centini, N. Akozbek, A. D'Orazio, J. W. Haus, M. J. Bloemer, and M. Scalora, "Tailoring metallodielectric structures for superresolution and superguiding applications in the visible and near-IR ranges," *Phys. Rev. A* **77**, p. 033848, 2008.
16. R. Kotyński and T. Stefaniuk, "Multiscale analysis of subwavelength imaging with metaldielectric multilayers," *Opt. Lett.* **35**(8), pp. 1133–1135, 2010.